CrossMark

Seasonal climate signals (1990–2008) in a modern Soreq Cave stalagmite as revealed by high-resolution geochemical analysis

Ian J. Orland [a,*], Yuval Burstyn [b,c], Miryam Bar-Matthews [b], Reinhard Kozdon [a], Avner Ayalon [b], Alan Matthews [c], John W. Valley [a]

[a] WiscSIMS, Department of Geoscience, University of Wisconsin, 1215W Dayton St., Madison, WI 53706, USA
[b] Geological Survey of Israel, 30 Malchei Israel St., Jerusalem 95501, Israel
[c] The Institute of Earth Sciences, The Hebrew University, Givat Ram, Jerusalem 91904, Israel

ABSTRACT

High-resolution isotopic and geochemical analyses in a modern (1990–2008) Soreq Cave stalagmite are compared to instrumental records of rainfall and dripwater from the cave, with the aim of determining how seasonal-resolution climate information is transmitted to speleothem geochemistry. In situ, micron-scale analysis of oxygen isotope ratios ($\delta^{18}O$) and trace elements by ion microprobe in combination with a continuous, linear traverse of trace element concentrations by laser-ablation ICP-MS (LA-ICP-MS) allow the definition of geochemical pathways within the cave. Fluorescent banding, imaged by confocal laser fluorescent microscopy (CLFM), as well as $\delta^{18}O$ and trace element variations is used to define 18 annual growth increments. Reduced intensity of fluorescent banding and a change in trace element variability reflect the decrease in average rainfall from 628 mm/yr (1990–1998) to 433 mm/yr (1999–2008). During the wetter period before 1998, Pearson (r-value) and Spearman (ρ-value) correlation coefficients are >0.5 for ion microprobe analyses of the element pairings Sr–Y, Y–P, and Mn–Si. After the transition to the drier period in 1999, a different set of geochemical pairings have r- and ρ-values >0.5, including Mg–$\delta^{18}O$, Mg–Sr, and Sr–Ba. Principal component analysis of data from the adjacent LA-ICP-MS traverse identifies two primary underlying modes of trace element variability. Based on the ion microprobe correlations and principal component analyses, we suggest that a greater seasonal influx of particulate material into the cave during the wetter period (1990–1998) brought about greater P, Cu, Sr, Na, and U variability in the stalagmite. The co-variability of $\delta^{18}O$, Mg, Sr, and Ba is characteristic of the trace element pattern from the drier period (1999–2008) of growth when particulate transport is reduced. These findings support a two-reservoir model of Soreq Cave dripwaters. One reservoir displays a well-mixed "baseline" with a decadal residence time that supplies water to the cave year-round, probably from fine pores or grain-boundary films in the vadose zone. The second reservoir is seasonal rainwater enriched in organic acids, colloids, and small particles and is rapidly transmitted to the cave. Finally, the similar patterns of fluorescence intensity, P, and Cu concentrations support the hypothesis that fluorescent bands in Soreq Cave speleothems are caused by the influx of organic colloids.

© 2013 Elsevier B.V. All rights reserved.

1. Introduction

Cave deposits (speleothems) often preserve climate information in their geochemistry. Measurements of oxygen and carbon isotope ratios ($\delta^{18}O$, $\delta^{13}C$) as well as trace element concentrations in carbonate speleothems are used to decipher both paleoclimate

and paleoenvironmental conditions (Fairchild et al., 2000; Richards and Dorale, 2003; McDermott, 2004; Fairchild et al., 2006; Baldini et al., 2008; Cheng et al., 2009; Lachniet, 2009; Cheng et al., 2012). The need to improve the continental paleoclimate record, combined with innovations in high spatial-resolution geochemical analyses, has resulted in development of seasonal-resolution climate records from speleothems. Multiple in situ analytical techniques permit seasonal-resolution analyses: laser-ablation inductively-coupled-plasma mass-spectrometry (LA-ICP-MS) and synchrotron radiation micro X-ray fluorescence for trace element analyses; ion microprobe for $\delta^{18}O$ and trace element analyses (Fairchild et al., 2001; Finch et al., 2001; Huang et al., 2001; Kuczumow et al., 2001; Treble et al., 2003, 2005; Borsato et al., 2007; Orland et al., 2009; Frisia et al., 2012). High spatial-resolution records of trace elements in speleothems reflect seasonal changes in both cave atmosphere and hydrology that respond to regional climate

(Treble et al., 2003; Borsato et al., 2007; Mattey et al., 2010; Wong et al., 2011). Likewise, high spatial-resolution analyses of $\delta^{18}O$ add seasonal rainfall information (Johnson et al., 2006; Orland et al., 2009, 2012).

Studies that combine seasonal-resolution analyses of trace elements and $\delta^{18}O$ (Johnson et al., 2006) are uncommon because conventional drill-sampling techniques for $\delta^{18}O$ analysis are typically incapable of sampling at the required spatial resolution. Recent advances in the accuracy and precision of $\delta^{18}O$ analyses by the ion microprobe at the WiscSIMS Laboratory, University of Wisconsin-Madison (UW-Madison), allow users to resolve subtle $\delta^{18}O$ variability in carbonate paleoclimate proxy records on a 10 μm scale (Weidel et al., 2007; Orland et al., 2009; Valley and Kita, 2009; Kozdon et al., 2011; Orland et al., 2012). With this technique, it is now possible to measure the variability of $\delta^{18}O$ in speleothems at a finer spatial resolution than trace element measurements by LA-ICP-MS; seasonal-scale climate interpretations that integrate analyses of $\delta^{18}O$ and trace elements are now viable in many more speleothems.

This study combines high-resolution data from several techniques in order to examine the coupled behavior of $\delta^{18}O$ and trace elements in a modern speleothem (sample "5–3b") from the semi-arid Soreq Cave locality in Israel (31°45.35′N, 35°1.35′E; Fig. 1). Measurements by LA-ICP-MS (continuous trace element traverse) and WiscSIMS ion microprobe (trace element and $\delta^{18}O$ spot analyses) are paired with imaging by confocal laser fluorescent microscopy (CLFM). The results will provide a basis for paleoclimate interpretations of both $\delta^{18}O$ and trace element records from Soreq Cave, which is a well-studied site in the Judean Hills ~400 m above sea level and 40 km inland from the Mediterranean Sea, as well as other caves in semi-arid regions (Bar-Matthews et al., 1997; Ayalon et al., 1998; Kaufman et al., 1998; Ayalon et al., 1999; Bar-Matthews et al., 1999; Matthews et al., 2000; Ayalon et al., 2002; Bar-Matthews et al., 2003; Kolodny et al., 2003; McGarry et al., 2004; Affek et al., 2008; Bar-Matthews and Ayalon, 2011).

Prior work on Soreq Cave speleothems at WiscSIMS used CLFM imaging of fluorescent bands to guide sub-annual-resolution ion microprobe analyses of $\delta^{18}O$ (Orland et al., 2009, 2012). Coupled variability of fluorescence and $\delta^{18}O$ values was first identified across what were interpreted as annual growth bands in a Late Holocene speleothem (Orland et al., 2009). In that study, it was proposed that fluorescent bands were caused by organic compounds like humic and fulvic acids that were flushed into the cave during an annual winter wet-season. Orland et al. (2009) show that the sharp onset of each fluorescent band coincides with a drop in speleothem $\delta^{18}O$ that resembles the modern seasonal variability in dripwater and rainfall $\delta^{18}O$ values; modern values of rainfall $\delta^{18}O$ and dripwater $\delta^{18}O$ are lowest from November to April when >95% of annual rainfall occurs (Fig. 2). Cave monitoring at Soreq shows that as the winter wet-season ends, the source of dripwater gradually shifts to a high-$\delta^{18}O$ "baseline" vadose-zone reservoir (Ayalon et al., 1998) that is suggested to have fewer organic colloids in suspension (Orland et al., 2009). Based on this evidence, Orland et al. (2009) suggested that regular, sawtooth variability of $\delta^{18}O$ and fluorescence observed in Holocene Soreq speleothems mark annual growth bands; the gradual increase of $\delta^{18}O$ across each band accompanies a decrease in fluorescence and ends with an abrupt return to low $\delta^{18}O$ values at the onset of the next winter wet-season and bright fluorescent band.

Here we seek to further test the hypothesis that coupled variability of fluorescence and $\delta^{18}O$ delineate annual growth bands and rainfall amounts in a detailed analysis of modern stalagmite 5–3b. The age of sample 5–3b is constrained by its growth on a man-made object placed in Soreq Cave in 1990; the sample was collected in 2008. Because the maximum age of sample 5–3b is known, we can: (1) test the hypothesis that the fluorescent bands are annual markers, and subsequently (2) compare speleothem geochemistry to instrumental records of both rainfall above Soreq and dripwater within the cave. In addition, we use correlation statistics and principal component analysis to assess the co-variability of $\delta^{18}O$, trace elements, and fluorescence measured in sample 5–3b (e.g. Borsato et al., 2007; Wassenburg et al., 2012). These comparisons allow us to evaluate the response of the geochemistry of 5–3b to changes in annual rainfall amount and test whether organic colloids are the cause of fluorescent banding in the sample.

2. Materials and methods

Sample 5–3b is a stalagmite that formed on the base of a stationary drip-collecting apparatus placed in Soreq Cave in July 1990. The stalagmite grew underneath a soda straw-type stalactite that had a consistent external morphology over the study period and dripped year-round. Regular observations of soda straw drip-rates at this site since 2009 have an average of 1.4 ml/day (Burstyn, 2013). Sample 5–3b was removed from Soreq in August 2008, and then cut in half along its vertical growth axis. The cross section of 5–3b prepared for analysis measures 5.4 mm along the vertical axis and 10.0 mm across the base. Fig. A.1 in the Supplementary online material shows optical imagery of 5–3b
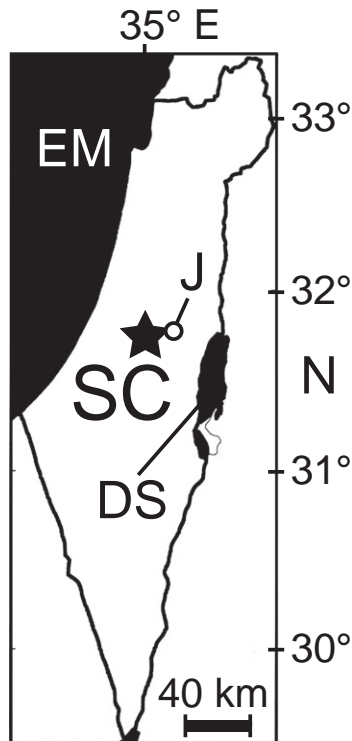

Fig. 1. Map of Israel with the location of Soreq Cave (SC, star). J = Jerusalem, EM = Eastern Mediterranean Sea, DS = Dead Sea.
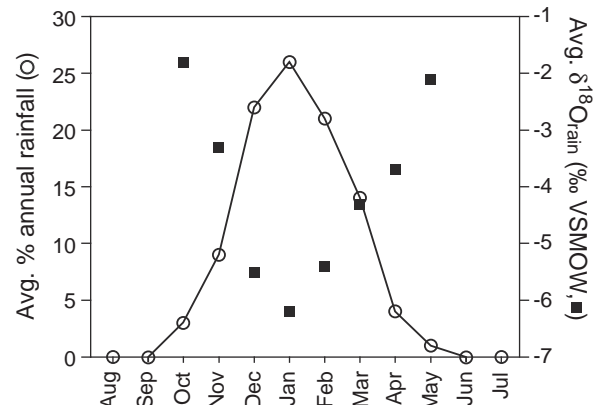

Fig. 2. Average monthly rainfall totals and $\delta^{18}O$ values measured above Soreq Cave from 1995–2008 (based on Ayalon et al., 1998; Orland et al., 2009).

before and after being sectioned for casting in a 25 mm-diameter epoxy mount. The 25 mm epoxy round, which includes 3 grains of UWC-3 (calcite standard, $\delta^{18}O = 12.49‰$ VSMOW; Kozdon et al., 2009), was ground and polished at UW-Madison using diamond paste in a progression from 6 to 1 μm grits. The final polish was attained with a colloidal alumina (0.05 μm) solution. Following the casting and polishing processes, *in situ* X-ray diffraction analyses with 100 μm spot-size at UW-Madison showed that 5–3b is predominantly calcite; no aragonite was detected (Fig. A.2). Further sample preparation details are described in Orland et al. (2012).

2.1. Confocal laser fluorescent microscopy

Following polishing, 5–3b was imaged by confocal laser fluorescent microscopy (CLFM) at the UW-Madison Keck Bioimaging Lab with a Bio-Rad MRC-1024 scanning confocal microscope. Fluorescence was stimulated with a 40 mW laser (488 nm wavelength), and a filter isolated the emitted wavelengths between 505 and 539 nm — the green portion of the visible spectrum. A series of overlapping images were collected with a $10\times$ objective lens ($100\times$ total magnification, 959×1199 μm field of view) in order to generate a stitched map of the entire sample surface. Because we are unaware of a method to standardize fluorescence intensity during CLFM imaging, the focal-plane depth, laser power, and signal gain were held constant in order to normalize intensity measurements; for this reason, interpretation of fluorescence variability is limited to relative – not absolute – intensity values from the CLFM images. Along with reflected-light images at the same scale, the CLFM map was used to identify growth bands and target spots for $\delta^{18}O$ and trace element analysis by ion microprobe.

2.2. Ion microprobe analysis

Ion microprobe analysis of $\delta^{18}O$ in 5–3b followed the methodology established in earlier work using the CAMECA ims-1280 at the WiscSIMS lab, UW-Madison (Orland et al., 2009, 2012). Before analysis, the epoxy mount was cleaned in two successive 30 s sonication sessions, the first in ethanol and the second in distilled water. Next, a gold coat of ~60 nm thickness was applied to the polished surface to alleviate sample charging during ion microprobe analysis. A focused primary beam of $^{133}Cs^+$ ions was used to sputter each analysis pit *in situ*. The $\delta^{18}O$ analysis pits were 1 μm deep and oval-shaped, with the long dimension varying for different sessions from 10 to 15 μm depending on both primary-beam tuning and Cs-source conditions. Both $^{18}O^-$ and $^{16}O^-$ ions were collected by Faraday cups in multicollection mode. Using the standard-sample-standard bracketing technique outlined by prior workers (Kita et al., 2009; Kozdon et al., 2009; Valley and Kita, 2009), the average spot-to-spot reproducibility for the $\delta^{18}O$ analyses of UWC-3 calcite standard run with sample 5–3b was ±0.30‰ (2 standard deviations, s.d.; see the Supplementary material, Table A.1).

This study is the first to report a suite of trace element concentrations in a carbonate from the WiscSIMS ion microprobe. We report elemental concentrations of Mg, Si, P, Mn, Fe, Zn, Sr, Y, and Ba (Table A.2). A 1.0 nA primary beam of O^- ions with an accelerating voltage of 13 kV was generated from a duoplasmatron source and focused onto the sample surface. Sputtered secondary ions with a positive charge were accelerated across a 10 kV potential into the double-focusing mass spectrometer. Each spot analysis took 10 min and included: pre-sputtering to ablate the Au coating and stabilize secondary-ion emission (60 s), automatic beam centering (60 s), and five 90 s cycles of the magnet scanning through a range of masses (6.5–138). Non-peak positions were included in each analytical cycle at masses 6.5, 6.8, and 131 in order to allow the magnet to stabilize either after completing a cycle (6.5, 6.8) or when jumping a large gap in mass (131). Each analyzed mass was measured for either 2.0 s (Si) or 2.96 s (all others) followed by a 2.0 s waiting period. Ions of each mass were counted by the center-axis electron multiplier except for $^{40}Ca^+$ ions, which were directed into a center-axis Faraday cup

to avoid saturating the electron multiplier. The count rate measured for each element during a cycle was normalized to the count rate of ^{40}Ca measured in that same cycle. For ^{24}Mg, ^{31}P, ^{55}Mn, ^{57}Fe, ^{88}Sr, ^{89}Y, and ^{137}Ba, the average of ^{40}Ca-normalized count rates from all five cycles was used to calculate elemental concentrations. Decreasing count rates observed in the first 3 cycles of ^{28}Si and ^{64}Zn measurements, perhaps due to surface contamination, are removed from consideration so that for these elements only the final two cycles with stable count rates were averaged for the concentration calculations.

To avoid variability in matrix effects that would stem from using NIST glass as a standard, we used the UWC-3 calcite standard to calibrate ion microprobe measurements of trace elements in 5–3b. We established the trace element profile of UWC-3 from a combination of electron microprobe analyses at UW-Madison (see Supplemental material in Kozdon et al., 2009), LA-ICP-MS analyses at The Hebrew University-Jerusalem (HUJI; Table A.3), and ICP-atomic emission spectroscopy (AES; Perkin-Elmer Optima 5300) and ICP-MS (Perkin-Elmer ELA 6100) analyses by a commercial laboratory (Table A.3). The commercial laboratory analyzed UWC-3 and four working standards (SY-4, Natural Resources Canada; NBS-88B, US National Bureau of Standards; BCS-368 and GXR-3, Flanagan (1986)) by sodium peroxide fusion and cites an analytical precision of 10%. We report concentrations of nine elements in UWC-3: three from electron microprobe (Mg, Mn, Fe) and six from LA-ICP-MS (Si, P, Zn, Sr, Y, Ba). Results from the commercial laboratory show excellent agreement with these concentrations (Table A.4). Relative sensitivity factors (RSF) for WiscSIMS analyses of these nine trace elements in calcite were calculated using the average of five UWC-3 analyses at the beginning of the ion microprobe session (Table A.4). The RSF values are used to convert elemental count rates measured in 5–3b into elemental concentrations.

Following the analytical sessions, a thin gold coat was added to the sample surface to allow imaging of the pit-bottoms by scanning electron microscope (SEM). Ion microprobe pits from both trace element and $\delta^{18}O$ analyses were examined at high magnification ($>2500\times$) for irregularities like inclusions, cracks, or epoxy. Each pit-bottom was classified as "regular," "intermediate," or "irregular" (Tables A.1 and A.2). For trace element analyses, the irregular pits (n = 3) do not appear to have systematic offsets for any element. Therefore, all trace element analyses are included in our interpretations.

Oxygen isotope analyses are screened in two different ways. First, analyses with anomalous secondary-ion yields are excluded (Kozdon et al., 2009, 2011; Orland et al., 2012). As with the determination of spot-to-spot reproducibility, a standard-sample-standard technique is used to calculate the "percent yield" of each $\delta^{18}O$ analysis relative to the bracketing standard measurements. Analyses with anomalous ion yield values relative to other pits measured in the same session are assumed to reflect a sample abnormality (e.g. a non-carbonate inclusion). Because the range of "percent yield" values for each analysis session is dependent on the primary beam condition, an accepted range of percent yield is defined for each session using the Tukey outlier definition (Tukey, 1977). The accepted range of percent yield in the first analytical session was 94.3–99.3% and 91.1–101.5% in the second analytical session. A total of 12 $\delta^{18}O$ analyses fall outside of the secondary yield cutoff values (Table A.1). These analyses, which represent less than 6% of the 231 sample analyses, are excluded from further consideration.

Oxygen isotope analyses are then screened by SEM imaging. A total of 14 $\delta^{18}O$ pits classified as irregular (Table A.1) are removed from the plots and discussion presented below.

2.3. LA-ICP-MS analysis

LA-ICP-MS analysis of 5–3b was completed at HUJI using a New Wave Research UP-193FX laser ablation system with a custom-built, He-purged "super-cell" (Dvir and Kessel, unpublished results). The HUJI laser-ablation set-up is coupled with an Agilent Technologies 7500 series ICP quadrupole mass spectrometer for high-precision

measurements of elemental concentration. The analytical traverse is comprised of two co-axial laser passes, the first with a low-power (50% laser power, 30 Hz, 10 μm/s stage speed) 100 μm-diameter beam that removed ~5 μm of sample to "pre-clean" the surface. The second pass, for trace element analysis, used a higher power (65% power, 10 Hz, 4 μm/s stage speed) 55 μm-diameter beam that removed a further 10 μm of sample (Fig. A.3). Elemental counts in the ICP-MS were totaled 3 times/s so that each data point represents an integration of elemental counts from the 55 μm laser spot as it advanced ~1.3 μm. Imaging of an abruptly-terminated laser traverse by reflected-light profilometer (Fig. A.4) indicates that laser ablation rate is relatively consistent across the target such that material at the trailing edge of the laser is ablated at approximately the same rate as the leading edge. Thus, the resulting traverses can be likened to a 55 μm moving-average calculated at 1.3 μm intervals.

Concentrations of 11 elements (^{23}Na, ^{24}Mg, ^{29}Si, ^{31}P, ^{55}Mn, ^{63}Cu, ^{66}Zn, ^{88}Sr, ^{138}Ba, ^{208}Pb, and ^{238}U) were calculated in sample 5–3b using five bracketing analyses – two before and three after the traverse – of a chip of NIST-610 glass standard mounted adjacent to the sample in the super-cell. Each NIST-610 analysis is comprised of a ~30 s (120 μm-long) traverse using the same analytical settings (no pre-clean) as described above. Data reduction was completed with the Iolite software package using ^{43}Ca as an internal standard (Hellstrom et al., 2008; Paton et al., 2011). Since a characterized carbonate standard did not exist, no matrix correction was made to the concentration values measured by LA-ICP-MS (Fig. A.5). Table A.3 suggests that no matrix correction is needed, because glass-standardized LA-ICP-MS measurements of UWC-3 show excellent agreement with the ICP-AES/MS results.

Since the environmental interpretations presented in this study are primarily based on patterns of trace element variability, it is important to show that relative concentration values measured by LA-ICP-MS across sample 5–3b are reproducible. We approach this issue in two ways. First, we demonstrate analytical reproducibility by calculating the 2 s.d. of elemental concentrations measured in the five bracketing NIST-610 analyses. Using ^{29}Si as an internal standard, the 2 s.d. of Na, Mg, P, Mn, Cu, Zn, Sr, Ba, Pb, and U concentration variabilities measured during the five NIST-610 analyses are <1% of the respective average concentrations (Table A.5). Second, we analyzed another LA-ICP-MS traverse parallel to the analytical traverse, offset laterally by 125 μm and without a pre-cleaning trench. The parallel traverse verifies both the elemental concentration and variability measured in the analytical traverse (Fig. A.6).

2.4. Principal component analysis

The trace element results from the continuous laser traverse are well-suited for principal component analysis (PCA; Mix et al., 1986; von Storch and Zwiers, 1999). PCA evaluates the time-series components of empirical orthogonal functions, which reveal common variability in multiple, concurrent datasets. PCA was performed with MATLAB (2010) software using the built-in `princomp` function. We applied the PCA technique to z-score normalizations (data normalized to have mean = 0, s.d. = 1) of trace element transects and a profile of fluorescence intensity that was measured parallel to the laser trench.

The fluorescence intensity data used in the PCA was obtained from a group of stitched CLFM images that follow the LA-ICP-MS traverse. The fluorescence profile was generated in ImageJ, an open-source image processing software (Rasband, 2012), by averaging the pixel brightness intensity (on a grayscale from 0–255) of a 5-pixel-wide traverse that is offset 75 μm from the laser trench. We used the AnalySeries software (Paillard et al., 1996) to re-sample the fluorescence profile by linear interpolation in order to match the sampling resolution of the LA-ICP-MS data, a requirement for PCA.

3. Results

3.1. Fluorescent banding

Fig. 3 shows CLFM imaging of the polished analytical surface – a vertical section – of stalagmite 5–3b. Concentric fluorescent banding is evident along the entire analytical traverse (Fig. 4), which is aligned parallel to the vertical growth axis. There is a striking transition from distinct, bright fluorescent banding in the older ("inner") portion of the sample to subtle fluorescent banding in the more porous younger ("outer") portion. The crystal fabric of the stalagmite also changes between the inner and outer portions. Calcite crystals in the inner portion are blocky with low porosity, while the outer portion is highly porous with a dendritic calcite fabric that radiates away from the growth surface.

A discontinuity between the inner and outer portions is highlighted by a dashed line in Fig. 3 and appears to be a healed fracture. Non-fluorescent calcite crystals that are interspersed with voids (~100 μm in diameter) act as infill above the dashed fracture. Laterally continuous growth bands cap the infill and mark the transition to subtle fluorescent banding in the outer portion. The white bracket in Fig. 3 shows an area of "indistinct" banding where it is difficult to trace continuous fluorescent bands. The indistinct banding occurs immediately before the abrupt transition to the subtle fluorescent banding regime.

3.2. $\delta^{18}O$ analyses

Values of $\delta^{18}O$ measured by ion microprobe span a range of 5.1‰, from 22.5 to 27.6‰ (VSMOW). The average spot-to-spot precision measured for UWC-3 bracketing standards is ±0.30‰ (2 s.d.). Fig. 4A illustrates the location of 213 $\delta^{18}O$ analyses made on sample 5–3b (white circles). Fig. 4B shows the $\delta^{18}O$ values of each measurement plotted against distance (projected on the LA-ICP-MS traverse). Tabulated results of each ion microprobe $\delta^{18}O$ analysis are reported in the data repository, Table A.1. Fig. A.7 is a high-resolution map of the analytical traverse with each ion microprobe analysis labeled.

Seven analysis pits were targeted along a single fluorescent band (Fig. 3) in order to confirm the consistency of $\delta^{18}O$ values measured along a single band. As in Orland et al. (2012), along-band analyses are used to assess the influence of variable porosity on the reproducibility of $\delta^{18}O$ measurements. We chose to target a distinctive fluorescent band (Fig. 3) in the outer portion of the sample. The seven $\delta^{18}O$ measurements along the targeted band in 5–3b have a 2 s.d. of 0.31‰, nearly identical to the 2 s.d. of the bracketing UWC-3 standard (0.30‰). Furthermore, their secondary ion yields vary from 96–98% of the bracketing standards, well within the yield-cutoff values of 94.3 and 99.3% for that analytical session. These results demonstrate the along-band continuity of $\delta^{18}O$ values in sample 5–3b.

3.3. Trace element analyses

Trace element concentrations from both ion microprobe and LA-ICP-MS analyses are shown in Fig. 4 for four elements: Mg, Sr, Si, and P. Fig. A.5 includes trace element profiles for all 11 elements measured by LA-ICP-MS. Concentration data from the 42 ion microprobe analyses of trace elements are reported in Table A.2.

We note that the mass used to measure Mn concentration by LA-ICP-MS (^{55}Mn) has a common isobaric interference in ICP mass spectrometers (^{40}Ar^{15}N$^+$ is formed in the Ar plasma; Jochum et al., 2012). LA-ICP-MS measurements of Mn in sample 5–3b are validated by comparable ion microprobe results. Since the calibration of ion microprobe measurements of Mn in 5–3b is based on electron microprobe analysis of Mn in UWC-3 (Kozdon et al., 2009), the ion microprobe measurements of Mn in sample 5–3b provide independent confirmation of the LA-ICP-MS transect.
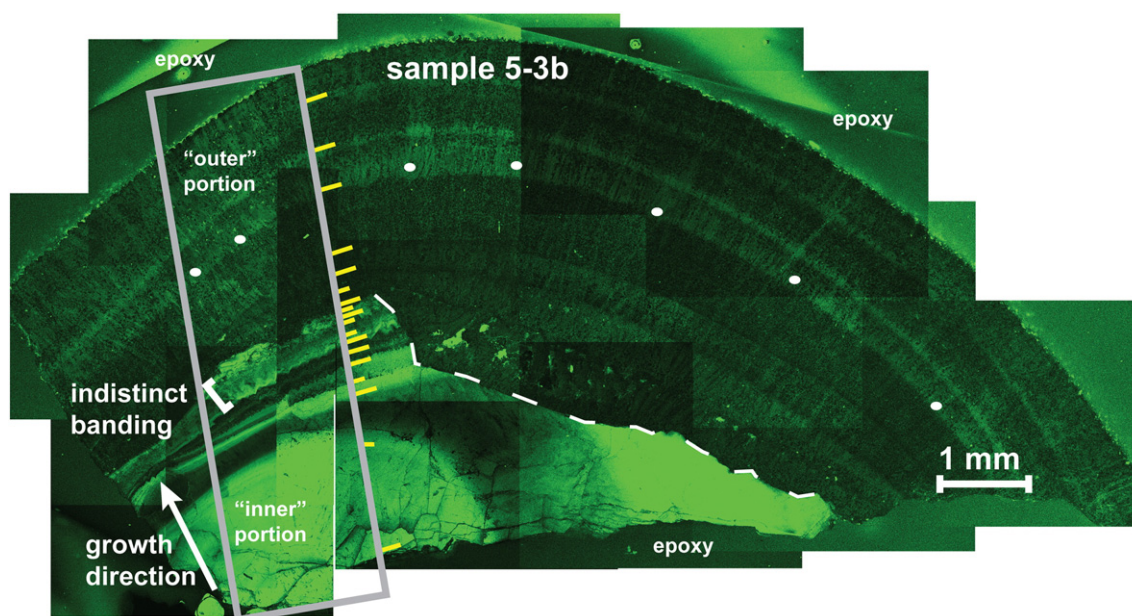
Fig. 3. CLFM image of the vertical polished surface ("inner" portion = bottom of sample, "outer" portion = top) of sample 5–3b, tiled together from smaller images. The dashed white line highlights a growth discontinuity, which appears to be a healed fracture (see text, Section 3.1). The rectangle outlines the area of sample 5–3b that includes the analytical traverse displayed in Fig. 4. Yellow hashes mark the annual growth increments as interpreted in Fig. 4. The white bracket shows the location of the indistinct banding that occurs immediately prior to the transition to more subtle fluorescent bands (Section 3.1). White ovals indicate the spot locations (pit size not to scale) for ion microprobe analyses of $\delta^{18}O$ along a single band (Section 3.2). Note that the growth rate of 5–3b is not a linear function of annual band widths along the analytical traverse because the analytical surface bisects a half-spherical sample.

3.4. Principal component analysis and correlation results

The PCA results illustrated in Fig. 5 and discussed below incorporate 12 variables. They are: (1) a record of fluorescence intensity across 5–3b as measured by CLFM and (2) 11 LA-ICP-MS elemental transects with signals discernable above background noise (Na, Mg, Si, P, Mn, Cu, Zn, Sr, Ba, Pb, U).

PCA results are displayed in Fig. 5 in three manners: the "percentage of total variance" explained by each principal component, the sample "scores", and the variable "loadings." We briefly outline their meaning here. PCA redistributes the variance observed in our 12 variables into 12 orthogonal axes called "principal components" (PC) that are oriented according to patterns of co-variation in the original data (Davis, 2002). In concept, the principal components reflect underlying forcing mechanisms.

Each of the PCs describes a "percentage of the total variance" observed in the original data, and they are ranked according to this value (i.e. the first principal component, PC1, explains the highest percentage of total variance). Each PC is described by a time-series of normalized "scores" that defines a pattern of variability that is unique to that principal component. For every PC, all 12 of the input variables are assigned a "loading" on a scale from −1 to 1 that indicates how well each variable correlates to the PC. A loading value of one denotes perfect positive correlation to a PC, while a negative loading value signifies an inverse correlation. In Fig. 5D–F, the loadings are plotted for each element relative to the first three PCs. Different classes of elements with shared geochemical properties are outlined in color to ease visual comparison. Alkaline earth metals are highlighted in blue (Mg) and red (Sr, Ba), while colloid- and silicate-borne elements are highlighted in green (P, Cu) and yellow (Si, Mn), respectively.

The percentage of total variance explained by the first three PCs are 26%, 24%, and 14%. Together, they yield a cumulative percentage of 64% of the total variance explained by all of the PCs. For each of the nine remaining PCs, the percentage of total variance is <8% and as such, these PCs are not discussed below as significant components of the LA-ICP-MS dataset.

Two tests verify the patterns of variability illustrated in Fig. 5 (Fig. A.8). First, we note that the large peaks in the scores of PCs 1–3 (Fig. 5A–C) correspond to high trace element concentrations near the upper edge of the indistinct layer (e.g. Sr; Fig. 4B) as well as at the very top of the sample. PCA of the LA-ICP-MS results minus the portions with exceptional trace element concentrations gives similar PC scores and elemental loadings to those illustrated in Fig. 5. The second test aims to assess the impact of the relatively wide band at the base of the sample on the PC patterns by removing the first 1000 µm of the analytical traverse from the PCA. Although this represents a 20% decrease in the analytical traverse, because there is little elemental variability in this section (see Fig. 4) the resulting PC scores and elemental loadings are again similar to those in Fig. 5.

In addition to PCA, a combination of three statistical conditions is used to identify significant correlations among geochemical variables in sample 5–3b: (1) Pearson r-value > 0.5, (2) respective p-value < 0.02, and (3) Spearman rank correlation ρ-value > 0.5. Both Pearson r-values and Spearman ρ-values are measured on a scale from 0 to 1 with higher values indicating increased correlation. The p-value indicates the probability on a scale from 0 to 1 that a higher value of Pearson's r-value could be obtained from a non-correlating dataset. Thus, low p-values indicate more significant r-values.

Pearson correlation coefficients (r-values; Johnson and Bhattacharyya, 2009) for the inner 16 and outer 22 trace element pits are tabulated in Table 1; correlations that meet all three conditions from above are given in bold. The dataset was subdivided into three portions (inner, indistinct, outer) based on the fluorescent banding in Fig. 3. The four pits analyzed within the indistinct banding layer are excluded from the correlations in Table 1; these four pits only served to mask correlation coefficients of the inner and outer datasets. In order to assess the correlation of each trace element to $\delta^{18}O$, we identified the $\delta^{18}O$ pit closest to the location of each trace element analysis. Although Fe and Zn concentrations were measured by ion microprobe, their respective correlation values are not included in Table 1 because they never meet the three significance conditions. All three statistical results for both ion microprobe and LA-ICP-MS analyses of sample 5–3b are available in Table A.6.
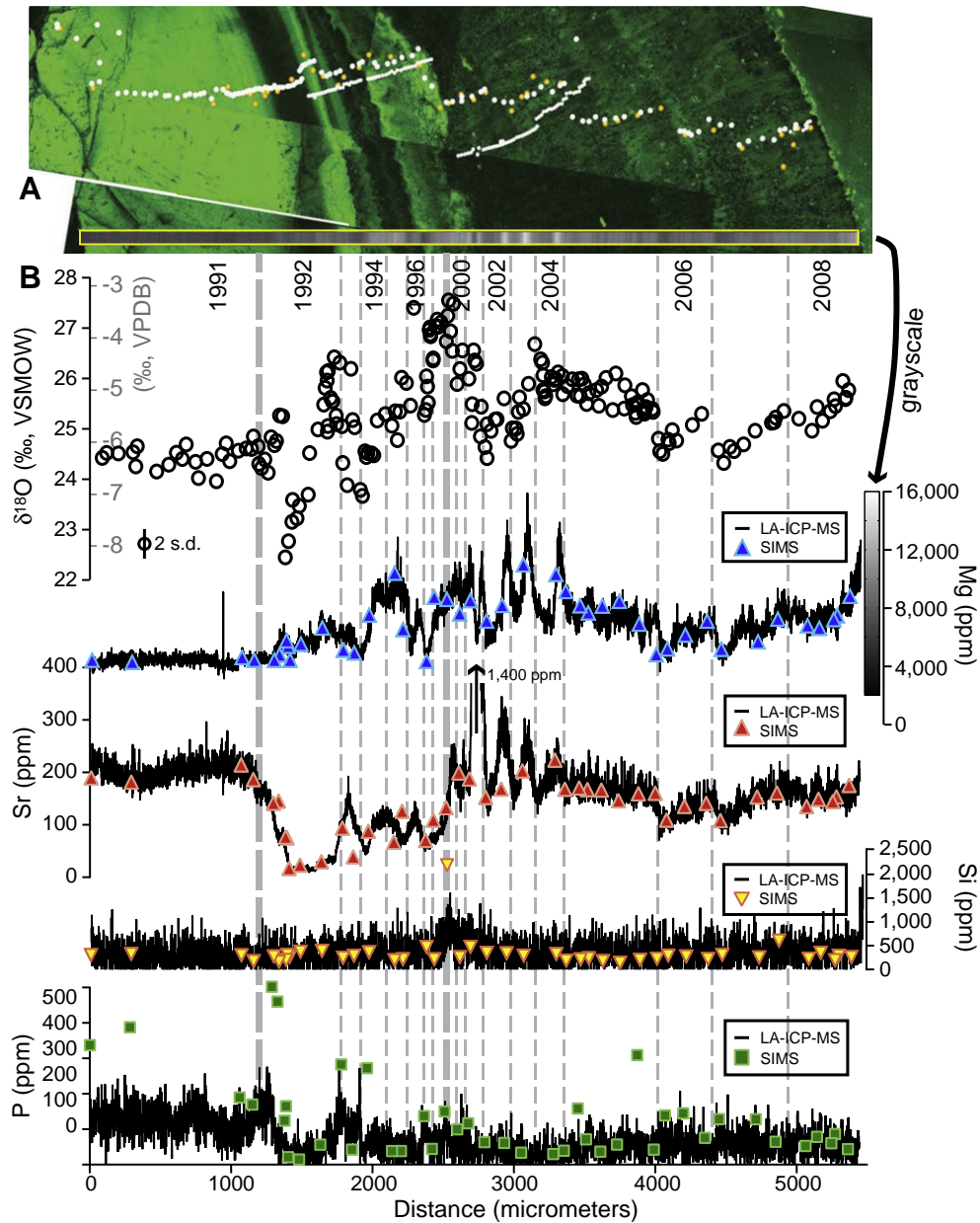
Fig. 4. Panel A is a stitched CLFM image of the area of analytical traverses shown in Fig. 3. Ion microprobe pits (10 μm diameter) for δ^{18}O are white circles, trace element pits are yellow circles. The location of the LA-ICP-MS laser trench (55 μm diameter spot, 1.3 μm step-size) is outlined with a yellow rectangle and the grayscale coloring within the traverse shows the Mg concentration. Panel B shows values of δ^{18}O, [Mg], [Sr], [P], and [Si]. The location of each ion microprobe pit was projected parallel to banding onto the laser traverse. For the four trace element profiles, spot analyses by ion microprobe are plotted as triangles with the continuous LA-ICP-MS traverse; there is good agreement between the two analytical methods. The grayscale legend for [Mg] applies to both panels A and B. The vertical dashed lines represent the inferred onset of winter wet-seasons; as described in Section 4.1.2 a water year is assigned to the growth between each dashed line. The two thicker dashed lines at 1992 and 1999 mark years with extreme rainfall δ^{18}O values, shown in Fig. 6.

4. Discussion

Earlier work compared δ^{18}O values measured by ion microprobe to fluorescence imaging by CLFM in two Soreq speleothems (34–4 ka and 2.2–0.9 ka) and proposed that: (1) fluorescent bands in the speleothems represent annual growth bands, and (2) fluorescence and δ^{18}O values observed within single annual growth bands record seasonal rainfall patterns like the distinct wet and dry seasons of the modern climate regime (Orland et al., 2009, 2012). The suite of fluorescence, δ^{18}O, and trace element results from modern sample 5–3b test these hypotheses and add to our understanding of micro-scale trace element variability within Soreq speleothems. This information will help to calibrate paired micro-analyses of δ^{18}O and trace elements in future investigations of speleothems from semi-arid environments.

4.1. Chronology of sample 5–3b

4.1.1. Fluorescent banding

The first step towards determining if fluorescent bands are annual is to count the number of fluorescent bands. Since the sample substrate was placed in the cave in July 1990 and sample 5–3b was collected in August 2008, we expect to see 18 annual bands assuming that all years are recorded.

In Fig. 3, we find 12 bands (marked by the longer yellow hashes) that are distinguished by laterally-continuous fluorescent boundaries. Identifying additional definitive bands from just the CLFM imaging is challenging; the six bands marked with shorter hashes in Fig. 3 are interpreted as annual based on further insight gained from the geochemical analyses discussed below. Therefore, although fluorescent imaging identifies a
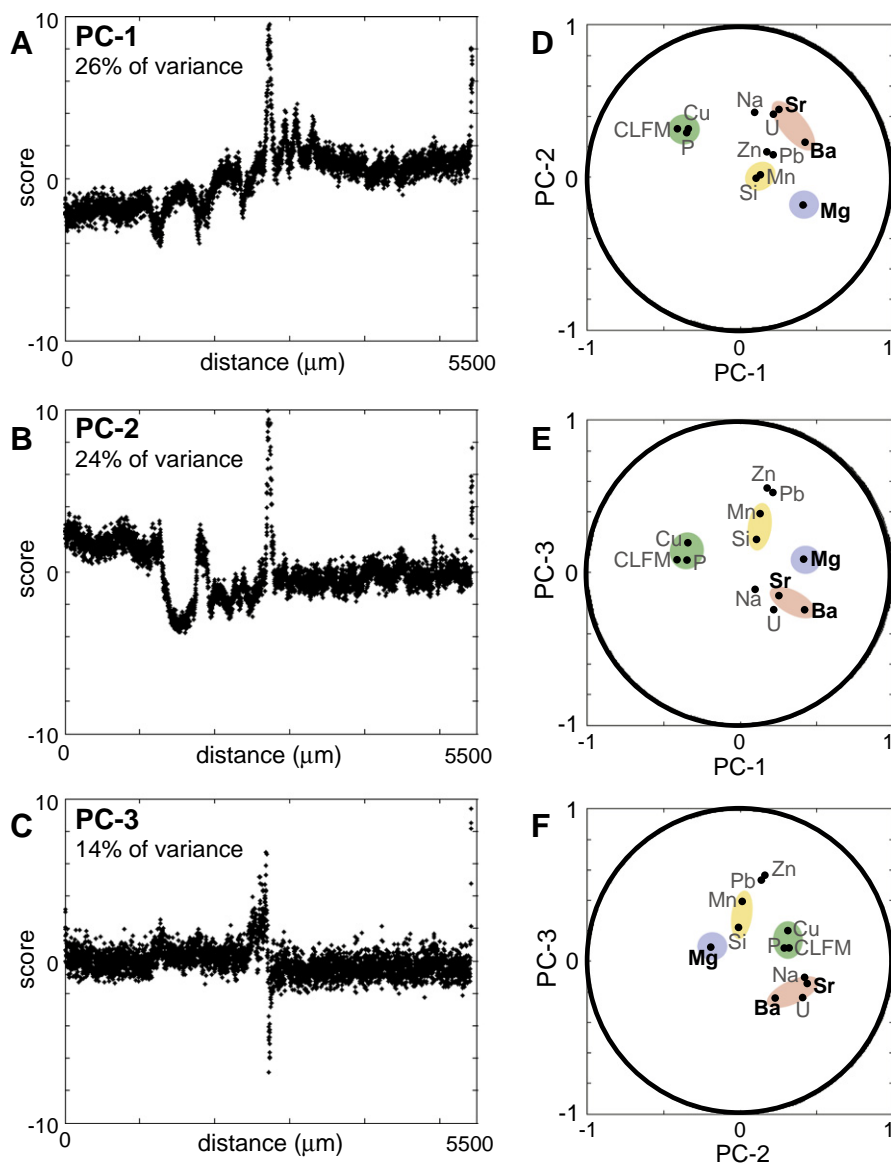
Fig. 5. PCA results for 12 datasets that traverse sample 5–3b, including 11 records of trace element concentration from LA-ICP-MS analysis (Na, Mg, Si, P, Mn, Cu, Zn, Sr, Ba, Pb, U) and one record of fluorescence intensity acquired by CLFM. Section 3.4 explains the PCA terminology. Panels A–C show the scores of PCs 1–3, respectively, plotted versus distance from the base of 5–3b. The percentage of total variance (%) represented by each PC is indicated in the upper-left corner of panels A–C. Panels D–F show the loadings of the 12 observed datasets for PC2 vs. PC1, PC3 vs. PC1, and PC3 vs. PC2, respectively. Since the sum of the squared loading values of a trace element on all of the principal components equals 1, the unit circles in panels D–F outline the maximum range of possible loadings. For example, if one trace element has a loading of 1 on any principal component, it must have a loading of zero on all others. Notable classes of elements are highlighted in color to facilitate comparison of their relative loadings; divalent cations are colored blue (Mg) and red (Sr, Ba), while elements transported by organic colloids or silicates are green (P, Cu) and yellow (Si, Mn). The similar variability of fluorescence intensity (CLFM) to that of P and Cu likely indicates that fluorescence in sample 5–3b is caused by P- and Cu-laden organic colloids. (For interpretation of the references to color in this figure legend, the reader is referred to the web version of this article.)

majority of the annual growth boundaries in 5–3b, geochemical analyses are needed to construct an 18-year age model.

Notably, the composite fluorescent image in Fig. 3 also shows that fluorescent bands in the inner portion of sample 5–3b are characteristically more intense than bands in the outer portion. Two interpretations are possible for the change in fluorescence. First, it is conceivable that whatever disturbance caused the discontinuity (dashed line in Fig. 3) also repositioned the man-made substrate so that sample 5–3b was directly beneath a new drip-point that inhibited fluorescence. Such changes are unlikely, especially since the vertical growth axis appears unchanged. Instead, we prefer a second hypothesis that the intense fluorescent bands indicate a wetter period when dripwaters above 5–3b carried an increased load of fluorescent material into the cave from the overlying soil. Correspondingly, the subtle banding in the outer portion indicates a drier period when either the supply or delivery of fluorescent material into the cave was suppressed. Geochemical analyses of

both sample 5–3b and rainwater collected above the cave allow us to scrutinize the suggested annual bands and test our explanation for the reduction in fluorescence intensity.

4.1.2. Anchor points from the δ18O record

At Soreq, Ayalon et al. (1998) show that the seasonal $\delta^{18}O$ signal in rainfall above the cave is imparted to dripwaters. This section further describes how the local rainfall $\delta^{18}O$ signal between 1990 and 2008 (Table A.7; Ayalon et al., 1998; Burg, 1998; Ayalon et al., 2004; Burstyn, 2013) is conveyed to Soreq speleothems and identifies prominent features in the rainfall record that can be used to anchor the chronology of 5–3b.

Fig. 2 illustrates the strong seasonal gradient of both rainfall amount and $\delta^{18}O$ values measured above Soreq Cave from 1995–2008; $\delta^{18}O$ values are lowest in the winter wet-season and highest in the fall and late spring. Since >95% of rainfall occurs between November and April,

Table 1

Correlation coefficients (Pearson's r) of geochemical data acquired by ion microprobe – including $\delta^{18}O$ values as well as Mg, Si, P, Mn, Sr, Y, and Ba concentrations – from two portions of sample 5–3b excluding the indistinct layer shown in Fig. 3. A shows the correlation of data between 0 and 2400 μm from the base of the sample. B includes data >2675 μm from the base of the sample. In each panel, the bolded, outlined values meet all three conditions that we use to identify significant correlations: (1) Pearson r-value > 0.5, (2) Pearson p-value < 0.02, and (3) Spearman rank correlation coefficient ρ-value > 0.5. Note that for a p-value of 0.1, the family-wise error rate (Dunn–Šidák correction; Sokal and Rohlf, 1995) for n = 28 is 0.0038. Complete correlation results are available in the supplementary material, Table A.6.

	$\delta^{18}O$	Mg	Si	P	Mn	Sr	Y	Ba
A) Pearson correlation coefficients (r) from inner portion of 5–3b.								
$\delta^{18}O$	1	0.27	−0.27	0.18	−0.07	0.34	0.11	0.37
Mg		1	−0.14	−0.36	−0.32	−0.31	−0.33	0.05
Si			1	−0.15	**0.66**	−0.34	−0.23	−0.20
P				1	0.05	**0.61**	**0.67**	0.28
Mn					1	0.17	0.09	0.24
Sr						1	**0.81**	**0.62**
Y							1	0.49
Ba								1
B) Pearson correlation coefficients (r) from outer portion of 5–3b.								
$\delta^{18}O$	1	**0.69**	−0.24	−0.25	−0.04	**0.74**	0.19	0.38
Mg		1	−0.05	−0.41	0.16	**0.81**	0.19	**0.57**
Si			1	−0.11	0.32	0.07	0.03	0.30
P				1	0.06	−0.34	−0.27	−0.34
Mn					1	0.19	0.18	−0.03
Sr						1	0.11	**0.57**
Y							1	−0.21
Ba								1

we use the notation "water year" to delineate wet seasons; a water year extends from October of one year through September of the next and is designated by the calendar year in which it ends. Fig. A.9 shows how the cumulative $\delta^{18}O$ of rain from each water year tracks the $\delta^{18}O$ of rainfall from that wet season. Thus, to simplify the presentation of rainfall data in both the tables and figures of this discussion, we reference values of rainfall amount and $\delta^{18}O$ integrated over entire water years.

Fig. A.9 also includes $\delta^{18}O$ values measured in dripwaters collected near sample 5–3b between 1991 and 1997 and starting again in 2001. These data (tabulated in Table A.8) have two important features that demonstrate how the rainfall $\delta^{18}O$ signal is transmitted into the cave. First, dripwater $\delta^{18}O$ is lowest during the wet season, as also observed in rainwater above the cave. Second, the minimum dripwater $\delta^{18}O$ values from each year track with annual rainwater $\delta^{18}O$. In a cave-wide dripwater survey, Ayalon et al. (1998) found that minimum dripwater $\delta^{18}O$ values each year were consistently ~1‰ higher than the annual rainfall $\delta^{18}O$ value. Fig. A.9 indicates a similar offset for dripwaters collected after 1998.

Critical for this study is the assumption that $\delta^{18}O$ values measured in sample 5–3b reflect near-equilibrium of $\delta^{18}O$ between calcite and dripwater. Recent modeling (Deininger et al., 2012) and experimental (Gabitov et al., 2012; Riechelmann et al., 2013) studies of isotope disequilibrium in speleothems suggest that seasonal variability of drip- and growth-rates could act to amplify the seasonal gradient of speleothem $\delta^{18}O$ relative to Soreq dripwater. Given the relatively low drip-rates in Soreq, however, these effects would impart <1‰ to the seasonal gradient — not enough to explain the observed variability. Furthermore, measurements of mass-47 CO_2 isotopologue anomalies (Δ_{47}) in modern Soreq speleothems indicate that modern calcite precipitated in near-equilibrium conditions for $\delta^{18}O$ although Δ_{47} values are not fully equilibrated (Affek et al., 2008). This accords with an earlier study of calcite precipitation in modern cave pools (Bar-Matthews et al., 1996).

With the knowledge that rainwater $\delta^{18}O$ variability is reliably transmitted to Soreq speleothems, two water years in the rainfall record stand out as being useful for correlating with the 5–3b $\delta^{18}O$ record

(Figs. 6 and A.9). The first is 1992, which had the highest annual rainfall amount over the period of interest (1020 mm) and the lowest $\delta^{18}O$ value of cumulative annual rainfall (−8.0‰, VSMOW). The second notable year is 1999, which had the lowest rainfall total of 215 mm and the highest cumulative $\delta^{18}O$ value, −4.5‰. Fig. 6 plots the rainfall totals and cumulative rainfall $\delta^{18}O$ values from 1991–2008 as well as all $\delta^{18}O$ values measured in 5–3b by ion microprobe. As in Fig. 4, the horizontal axis of Fig. 6 reflects the linear distance along the LA-ICP-MS traverse. We position the 1992 and 1999 water years (indicated with thick vertical dashed lines in Figs. 4 and 6) to match the portions of 5–3b with extreme $\delta^{18}O$ values.

In order to identify other years in the chronology, we look for the pattern of sawtooth $\delta^{18}O$ variability that earlier studies characterized in annual growth bands from Holocene Soreq speleothems (Orland et al., 2009, 2012). Using this approach, wet-season markers are assigned to the outer three growth bands (2006–08) as well as the four bands (1993–96) that follow the particularly wet 1992 water year (Fig. 4). In the intervening portion of the sample, which represents growth between 1997 and 2005, sawtooth patterns of $\delta^{18}O$ are apparent but fluorescent bands are less definitive. Therefore, trace element results are examined for complementary evidence of annual growth bands.
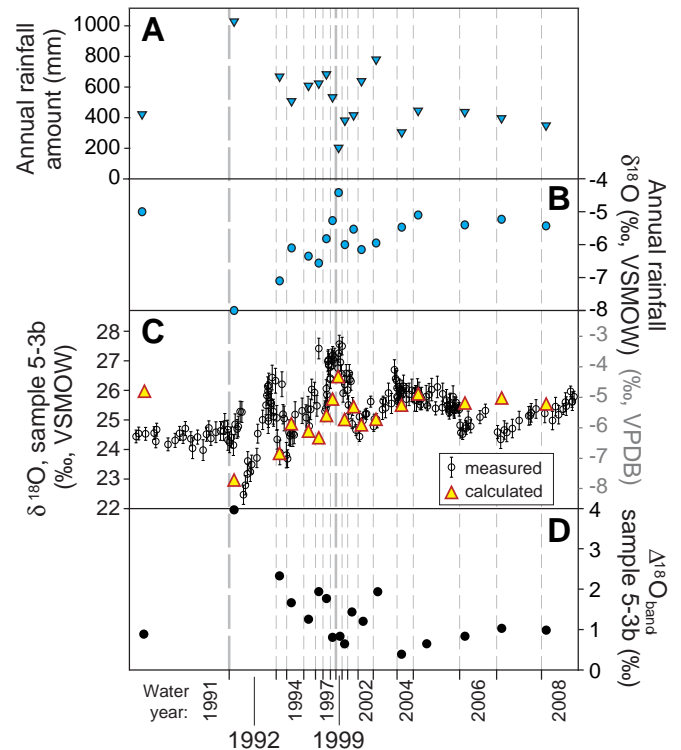
Fig. 6. Rainfall record from above Soreq Cave plotted against $\delta^{18}O$ values measured in sample 5–3b. Annually averaged rainfall $\delta^{18}O$ values (A) and amounts (B) are reported from water years 1991–2008. The time axis of each record is scaled to match the analytical traverse across 5–3b (C) according to the criteria explained in Section 4.1. The vertical dashed lines represent the onset of winter wet seasons; a water year is assigned to the growth between each dashed line. The two years with extreme annual $\delta^{18}O$ values, 1992 and 1999, are marked with thicker dashed lines and used to anchor the 5–3b $\delta^{18}O$ data to the instrumental record. Plotted alongside the $\delta^{18}O$ results from 5–3b in panel C are yellow triangles showing the predicted $\delta^{18}O$ of calcite precipitated at a cave-air temperature of 22.0 °C (Affek et al., 2008). The predicted $\delta^{18}O$ values are calculated using: (1) the annually averaged rainfall $\delta^{18}O$ values from panel A, which are corrected to dripwater $\delta^{18}O$ values by adding 1‰ (after Ayalon et al., 1998, 2004; Orland et al., 2009); and (2) the water–calcite fractionation factor for $\delta^{18}O$ from Tremaine et al. (2011), which is based on data from 15 modern speleothem studies. Panel D shows the difference between the highest and lowest $\delta^{18}O$ values ($\Delta^{18}O_{band}$) measured in each of the proposed annual bands. Note the similar variation of $\Delta^{18}O_{band}$ values and annual rainfall totals, illustrated further in Fig. 7.

4.1.3. Trace element variability and chronology

Many studies have identified records of annual trace element variability in speleothems (Fairchild et al., 2001; Treble et al., 2003, 2005; Johnson et al., 2006; Borsato et al., 2007; Fairchild and Treble, 2009). Together they provide valuable insight on the source and pathways of trace elements analyzed in sample 5–3b. For example, recent work (Borsato et al., 2007; Hartland et al., 2012) shows that P, Cu, Zn, Y, Pb, and other trace metals are commonly carried into the cave as adsorbed species on colloids, which likely includes organic particles from the overlying soil. The trace elements most commonly measured at sub-annual resolution in speleothem studies are the alkaline earth metals, Mg and Sr. They form divalent cations in solution, substitute for Ca^{2+} in calcite, and are particularly useful geochemical indicators in caves – like Soreq – that formed within dolomite bedrock (Table A.9).

Variability of Mg and Sr in dripwater is often attributed to changes in the amount of either groundwater–bedrock interaction or prior calcite precipitation (Fairchild and Treble, 2009; Schimpf et al., 2011; Wong et al., 2011). In drier conditions, the concentration of Mg and Sr in groundwater can be increased relative to Ca because: 1) longer periods of groundwater–bedrock interaction add higher proportions of Sr and Mg to the groundwater, or 2) calcite precipitation in rocks above the cave preferentially removes Ca from groundwaters. However, rather than attributing Mg and Sr variability in sample 5–3b to the seasonal influence of either or both of these mechanisms, we adopt the hydrological routing model of Fairchild et al. (2006) to explain trace element variability. They suggest that Mg and Sr concentrations in dripwater represent a mixture of groundwaters that have experienced different residence times or flow pathways within the vadose zone. This is the same model used to explain $\delta^{18}O$ variability in Soreq Cave dripwaters and speleothems (Ayalon et al., 1998; Kaufman et al., 2003; Orland et al., 2009).

Fig. A.9 shows that Mg concentrations in Soreq dripwaters (tabulated in Table A.8) adhere to the suggested model, with generally increasing concentrations following each wet season. Before using both Mg and Sr concentrations to identify annual bands in 5–3b, however, we take into account that: (1) in Soreq Cave speleothems, wind-blown dust is known to be a source of Sr (Ayalon et al., 1999; Bar-Matthews et al., 1999; Frumkin and Stein, 2004), and (2) Sr and Mg variability do not match in the inner portion of 5–3b (Fig. 4). Therefore, we focus on Mg variability to guide identification of the remaining annual bands in 5–3b.

Much like with $\delta^{18}O$, we interpret a sharp decrease in Mg concentration to indicate the onset of annual wet seasons; following the sharp decrease, a gradual increase in Mg concentration is expected as the relative contribution of longer-residence time groundwater grows. This interpretation corroborates the delineation of the 2006–08 growth bands identified by $\delta^{18}O$ variability. Furthermore, sawtooth variability of Mg is evident (although smoothed by the continuous laser traverse) in growth bands from 2000–05 where fluorescent bands were less conclusive. The remaining annual bands, 1997–99, are assigned by sawtooth $\delta^{18}O$ patterns that coincide with subtle Mg and fluorescence variability (Fig. 4).

4.2. Comparison of rainfall and speleothem $\delta^{18}O$ records

If we assume the age model constructed in the previous section is accurate, we can test the hypothesis of Orland et al. (2009) who suggest that the range of $\delta^{18}O$ in each band of a Late Holocene speleothem is a proxy for rainfall amount. They define a variable, $\Delta^{18}O = \delta^{18}O(\text{dark calcite}) - \delta^{18}O(\text{bright calcite})$, to describe the $\delta^{18}O$ range in individual growth bands. Here, since annual growth bands are not defined solely on the basis of fluorescence, $\Delta^{18}O$ values are denoted as $\Delta^{18}O_{band}$ and refer to the range of $\delta^{18}O$ measured within the $\delta^{18}O$ sawtooth recorded in each growth band. Fig. 6D plots the $\Delta^{18}O_{band}$ value calculated for each band in 5–3b. Fig. 7 illustrates a very good correlation between $\Delta^{18}O_{band}$ values measured in 5–3b and annual rainfall totals from above the cave

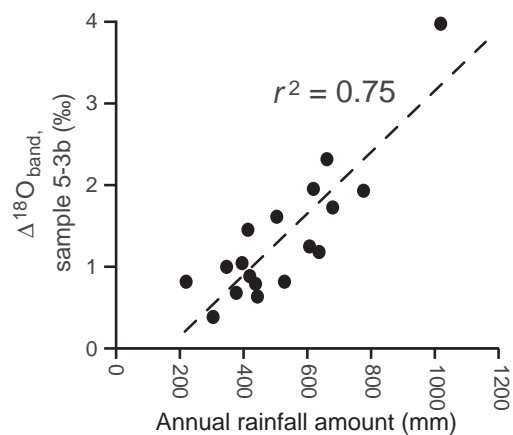**Fig. 7.** Illustrates the correlation between $\Delta^{18}O_{band}$ (range of $\delta^{18}O$ measured within each proposed annual band) and annual rainfall amount for sample 5–3b observed in Fig. 6D.

($r^2 = 0.75$), and thus supports the hypothesis that $\Delta^{18}O_{band}$ values are a proxy for annual rainfall amount in Soreq speleothems.

The correlation between $\Delta^{18}O_{band}$ and annual rainfall amount provides further insight into the two-reservoir groundwater system outlined above. According to the model of annual $\delta^{18}O$ variability described by Orland et al. (2009), the minimum $\delta^{18}O$ value of calcite in each annual band should approximately reflect the cumulative $\delta^{18}O$ of rainfall from the respective water year. In sample 5–3b, these values correlate with $r^2 = 0.42$. Similarly, the correlation between the minimum calcite $\delta^{18}O$ in each band and annual rainfall amount ($r^2 = 0.37$; Fig. A.10) is somewhat weaker than that between $\Delta^{18}O_{band}$ and annual rainfall amount ($r^2 = 0.75$, Fig. 7). If our age model is correct, we suggest that the stronger correlation of $\Delta^{18}O_{band}$ and annual rainfall amount is a result of some mixing between the short- and long-residence-time groundwater reservoirs that is weighted by the amount of wet-season rainfall, its $\delta^{18}O$ value, and the time since it fell above the cave.

4.3. Climate control of seasonal trace element variability

Building from the chronology of 5–3b proposed above, this study aims to identify signatures of seasonal climate within sub-annual trace element variability. Annual rainfall totals measured between 1991 and 2008 provide a benchmark against which to compare the geochemical data from sample 5–3b. In addition to the extreme wet and dry events used to anchor the chronology, the average amount of rainfall during a water year drops 195 mm from 628 to 433 mm between 1991–98 and 1999–2008. Ideally, the patterns of sub-annual geochemical variability reflect the shift from a wetter to a drier decade. One encouraging observation is the change in the character of fluorescent banding from the younger to older portion of sample 5–3b (Section 3.1); the distinctive fluorescence regimes likely reflect a change in dripwater chemistry that we can quantify with trace element analyses.

There is good agreement between ion microprobe and LA-ICP-MS analyses of Mg, Sr, Si, and P concentrations in sample 5–3b (Fig. 4). Similar plots for Ba, Mn, and Zn (Fig. A.5) also show agreement between concentration values measured by the two methods. Even before statistical analysis, common patterns of variability are clear within different classes of trace elements; one class is comprised of Mg, Sr, and Ba, another includes Si, Fe, and Mn.

4.3.1. Correlation of ion microprobe data

In their study of trace elements in speleothems, Wassenburg et al. (2012) emphasize elemental correlations with r-values > 0.5. Our study uses an additional condition to identify the significant elemental correlations that are highlighted in Table 1; the Spearman rank correlation coefficient (ρ-value; Johnson and Bhattacharyya, 2009) must also be > 0.5. By including the ρ-value requirement, we eliminate correlations

whose *r*-values are skewed by single extreme measurements (e.g. Mn vs. Fe).

The highlighted correlations in Table 1 are markedly different in the inner and outer portions of sample 5–3b. In the inner portion, the noted correlations include elements that are likely carried into the cave during relatively wet periods as either: (1) species adsorbed to organic colloids (P, Y) that may also cause fluorescence, or (2) detrital silicates, possibly including windblown dust (Sr, Mn, Si). In the outer portion, the notable correlations include elements that reflect the residence time of groundwater in the vadose zone before it reaches the cave (Mg, Sr, Ba, $\delta^{18}O$). The only correlation common to both inner and outer portions of the sample is between Sr and Ba, a logical result considering the similar ionic radii, valence states and partition coefficients (Day and Henderson, 2013) of these two species.

The switch in significant elemental correlations matches the change in rainfall measured above the cave and inferred from the shift to subtle fluorescent banding. During the relatively wetter conditions of 1991–98, both the distinct fluorescent banding along with P–Y–Sr and Mn–Si correlations indicate that wet-season dripwater included material washed into the cave from the near-surface. In contrast, when the rainfall record shows relatively dry conditions, subtle fluorescent banding and Mg–Sr–Ba–$\delta^{18}O$ correlations indicate that dripwaters had both a longer residence time in the vadose zone as well as a less-direct connection with the near-surface. The difference between the geochemical response recorded in the inner and outer portions of 5–3b is likely caused by the amount of suspended load carried in groundwater; trace elements that are preferentially transported by organic acids, colloids, and small particles – including wind-blown dust – are emphasized during periods of increased rainfall.

4.3.2. Principal components of LA-ICP-MS data

The panels on the left of Fig. 5 show the time series scores of the first three PCs and their respective percentages of total variance explained. The high percentage of variance explained by PC1 and PC2 relative to each of the remaining principal components suggests that PC1 and PC2 reflect the dominant modes of trace element variability in sample 5–3b. The panels on the right of Fig. 5 compare the loadings of 11 trace elements on each PC by plotting the loading of each element on PC2 vs. PC1, PC3 vs. PC1, and PC3 vs. PC2. These figures illustrate how different elemental concentrations display common patterns of variability; elements that plot near one another likely share common forcing mechanisms.

Each of the first three PCs is characterized by high loadings of different groups of elements. PC1 has high loadings of Mg, Sr, and Ba that likely reflect the effect of groundwater–bedrock interaction in the vadose zone. PC2 has high loadings of P, Cu, Sr, and U. These elements readily adsorb to colloids and organic acids (P, Cu) as well as wind-blown dust (Sr, U; Frumkin and Stein, 2004), suggesting that PC2 indicates the amount of particulate or colloidal components that are washed into the cave from the overlying soil. PC3 is the only remaining principal component that explains >8% of the total variance and has a pattern consistent with the inclusion of silicate particles in the indistinct banding layer; the highest positive elemental loadings in PC3 are Zn, Pb, Mn, and Si.

4.3.3. Characterizing groundwater reservoir compositions

Another notable feature of the PCA results is the relation of Mg to Sr and Ba in PCs 1 and 2. Fig. 5D shows that Mg, Sr and Ba have similar positive loadings on PC1, but Mg has a negative loading on PC2 while Sr and Ba have positive loadings. This conflicting pattern is comparable to the correlations seen in the ion microprobe data; strong positive correlations are observed between Mg–Sr and Mg–Ba in the outer portion of 5–3b, but these same correlations are weak in the inner portion (Table 1). We hypothesize that the first two principal components represent the same forcing mechanisms ascribed to the correlation data. As such, PC1 would illustrate the influence of groundwater residence time

on Mg, Sr, and Ba concentration, while PC2 reflects the amount of suspended material washed into the cave.

In order to test the similarity of the PCA and correlations results, we conducted PCA on the same inner and outer portions of 5–3b as used in the correlation treatment. The results (Fig. A.11) show that the first PC of the inner portion matches the variability of PC2 from the entire sample (Fig. 5B); this pattern is dominated by similar variability in Sr, Ba, Cu, P, and U. The first PC of the outer portion, however, is characterized by similar loadings of Mg, Sr, and Ba and has a comparable pattern of variability to PC1 of the entire sample (Fig. 5A). Thus, we are confident that PCs 1 and 2 of the entire sample represent the same forcing mechanisms used to explain correlations in the outer and inner portions, respectively (Table 1).

Given the proposed forcing factors for PCs 1 and 2, Fig. 5D is particularly interesting because it shows the loading of different elements with respect to both components. One feature that stands out is the strong positive loading of both Sr and Ba (outlined in red) on PCs 1 and 2. In this case, PCA illustrates how the two forcing factors overprint one another in the composite trace element record. On one hand, since Sr and Ba concentrate in groundwater that has decadal residence times in the dolomitic vadose zone, they reflect the proportion of vadose zone groundwater in dripwater (PC1). On the other hand, these elements are also delivered to the sample via small particles (likely wind-blown dust) that are flushed into the cave by intense wet season rains (PC2).

Therefore, trace element data reinforce the two-component hydrological routing model previously used to describe $\delta^{18}O$ and fluorescence variability in Soreq speleothems (Orland et al., 2009). While mixing of groundwater reservoirs is sufficient to explain the $\delta^{18}O$ variability of 5–3b, the seasonal delivery of particulate matter is critical to understanding the variability of trace elements like Sr, Ba, U, P, and Cu.

With regard to the influence of organic colloidal particles, we emphasize one final observation from the PCA results. Panels D–F of Fig. 5 illustrate the remarkably similar variability of fluorescence intensity and P and Cu concentrations across sample 5–3b; the loadings of P, Cu, and CLFM are grouped together (green outline) in each of the first three principal components. The similar patterns of variability support the hypothesis that organic molecules, which are vehicles for P, Cu, and other elements (Borsato et al., 2007; Fairchild and Treble, 2009; Hartland et al., 2012), cause the fluorescent banding in sample 5–3b.

5. Conclusions

We apply high-spatial-resolution analysis and imaging to a modern Soreq Cave stalagmite in order to evaluate the co-variation of $\delta^{18}O$, trace elements, and fluorescence on a seasonal scale. Records of rainfall amount and $\delta^{18}O$ collected above Soreq Cave during the period when the stalagmite grew allow us to test hypotheses regarding cave hydrology and the annual nature of fluorescent banding. The methods of this study could be used to acquire and interpret high-resolution geochemical data from other speleothems, including others from Soreq Cave. The results also demonstrate the benefits of a multi-proxy, high-resolution approach and lead to the following conclusions:

- Corroborating results were obtained from trace element analyses by ion microprobe and LA-ICP-MS.
- Fluorescent banding identifies most, but not all, of the annual growth bands we interpret from this sample. Oxygen isotope variability and trace element variability were considered in tandem with fluorescent banding in order to distinguish annual growth bands for each year of speleothem growth (water years 1991–2008).
- Both correlation analysis of ion microprobe data as well as principal component analysis (PCA) of LA-ICP-MS data reflect two modes of variability: (1) During the drier period from 1999–2008, muted fluorescent banding and the correlation of Mg, Sr, and Ba concentrations – likely sourced from the dolomitic country rock – suggest minimal infiltration of particulate matter; (2) During the wetter

period from 1991–1998, fluorescent bands are distinct and seasonal infiltration of organic colloids and small particles of wind-blown dust appears to accentuate the variability of P, Cu, Sr, Na, and U.

- Results support the two-reservoir model of Soreq Cave hydrology described by Orland et al. (2009). The first reservoir is stored in pores in the unsaturated zone where it accumulates divalent cations from the dolomite country rock, has a decadal residence time for $\delta^{18}O$ values in water, and supplies well-mixed "baseline" dripwater to the cave on a year-round basis. The second reservoir delivers wet season rainfall to the cave along more direct pathways and thus has a shorter, sub-annual residence time. PCA results also indicate that the variability of some trace elements (Sr, Ba, U, P, Cu) is overprinted by the delivery of particulate matter during intense wet season rains.

- Similar variability of P, Cu, and fluorescence intensity in a PCA of sample 5–3b data supports the hypothesis that fluorescent banding is caused by organic colloids washed into the cave from the overlying soil.

Supplementary data to this article can be found online at http://dx.doi.org/10.1016/j.chemgeo.2013.11.011.

Acknowledgments

References

Affek, H.P., Bar-Matthews, M., Ayalon, A., Matthews, A., Eiler, J.M., 2008. Glacial/interglacial temperature variations in Soreq cave speleothems as recorded by 'clumped isotope' thermometry. Geochim. Cosmochim. Acta 72, 5351–5360.

Ayalon, A., Bar-Matthews, M., Sass, E., 1998. Rainfall-recharge relationships within a karstic terrain in the Eastern Mediterranean semi-arid region, Israel: $\delta^{18}O$ and δD characteristics. J. Hydrol. 207, 18–31.

Ayalon, A., Bar-Matthews, M., Kaufman, A., 1999. Petrography, strontium, barium and uranium concentrations, and strontium and uranium isotope ratios in speleothems as palaeoclimatic proxies: Soreq Cave, Israel. The Holocene 9, 715–722.

Ayalon, A., Bar-Matthews, M., Kaufman, A., 2002. Climatic conditions during marine oxygen isotope stage 6 in the eastern Mediterranean region from the isotopic composition of speleothems of Soreq Cave, Israel. Geology 30, 303–306.

Ayalon, A., Bar-Matthews, M., Schilman, B., 2004. Rainfall isotopic characteristics at various sites in Israel and the relationships with unsaturated zone water. Geological Survey of Israel Reports, GSI/16/04. The Ministry of National Infrastructures, Jerusalem.

Baldini, J.U.L., McDermott, F., Hoffmann, D.L., Richards, D.A., Clipson, N., 2008. Very high-frequency and seasonal cave atmosphere PCO_2 variability: implications for stalagmite growth and oxygen isotope-based paleoclimate records. Earth Planet. Sci. Lett. 272, 118–129.

Bar-Matthews, M., Ayalon, A., 2011. Mid-Holocene climate variations revealed by high-resolution speleothem records from Soreq Cave, Israel and their correlation with cultural changes. The Holocene 21, 163–171.

Bar-Matthews, M., Ayalon, A., Matthews, A., Sass, E., Halicz, L., 1996. Carbon and oxygen isotope study of the active water–carbonate system in a karstic Mediterranean cave: implications for paleoclimate research in semiarid regions. Geochim. Cosmochim. Acta 60, 337–347.

Bar-Matthews, M., Ayalon, A., Kaufman, A., 1997. Late Quaternary paleoclimate in the eastern Mediterranean region from stable isotope analysis of speleothems at Soreq Cave, Israel. Quat. Res. 47, 155–168.

Bar-Matthews, M., Ayalon, A., Kaufman, A., Wasserburg, G.J., 1999. The Eastern Mediterranean paleoclimate as a reflection of regional events: Soreq Cave, Israel. Earth Planet. Sci. Lett. 166, 85–95.

Bar-Matthews, M., Ayalon, A., Gilmour, M., Matthews, A., Hawkesworth, C.J., 2003. Sea–land oxygen isotopic relationships from planktonic foraminifera and speleothems in the Eastern Mediterranean region and their implication for paleorainfall during interglacial intervals. Geochim. Cosmochim. Acta 67, 3181–3199.

Borsato, A., Frisia, S., Fairchild, I.J., Somogyi, A., Susini, J., 2007. Trace element distribution in annual stalagmite laminae mapped by micrometer-resolution X-ray fluorescence: implications for incorporation of environmentally significant species. Geochim. Cosmochim. Acta 71, 1494–1512.

Burg, A., 1998. Geochemistry and hydrology of perched carbonate aquifers in northern and central Israel. (Ph.D. Thesis) The Hebrew University, Jerusalem (178 pp. in Hebrew, English abstract).

Burstyn, Y., 2013. Multi-decade to seasonal climate change recorded by stable isotope and trace element variability in modern cave-waters and calcite of Soreq Cave, Israel. Geological Survey of Israel Reports, GSI/13/2013. The Ministry of National Infrastructures, Jerusalem.

Cheng, H., Edwards, R.L., Broecker, W.S., Denton, G.H., Kong, X., Wang, Y., Zhang, R., Wang, X., 2009. Ice age terminations. Science 326, 248–252.

Cheng, H., Zhang, P.Z., Spötl, C., Edwards, R.L., Cai, Y.J., Zhang, D.Z., Sang, W.C., Tan, M., An, Z.S., 2012. The climatic cyclicity in semi-arid central Asia over the past 500,000 years. Geophys. Res. Lett. 39, L01705.

Davis, J.C., 2002. Statistics and Data Analysis in Geology. John Wiley and Sons, New York (638 pp.).

Day, C.C., Henderson, G.M., 2013. Controls on trace-element partitioning in cave-analogue calcite. Geochim. Cosmochim. Acta 120, 612–627.

Deininger, M., Fohlmeister, J., Scholz, D., Mangini, A., 2012. Isotope disequilibrium effects: the influence of evaporation and ventilation effects on the carbon and oxygen isotope composition of speleothems — a model approach. Geochim. Cosmochim. Acta 96, 57–79.

Dvir, O., Kessel, R., 2013. The effect of cell geometry on alkali element fractionation during LA-ICP-MS analysis (Unpublished results).

Fairchild, I.J., Treble, P.C., 2009. Trace elements in speleothems as recorders of environmental change. Quat. Sci. Rev. 28, 449–468.

Fairchild, I.J., Borsato, A., Tooth, A.F., Frisia, S., Hawkesworth, C.J., Huang, Y., McDermott, F., Spiro, B., 2000. Controls on trace element (Sr–Mg) compositions of carbonate cave waters: implications for speleothem climatic records. Chem. Geol. 166, 255–269.

Fairchild, I.J., Baker, A., Borsato, A., Frisia, S., Hinton, R.W., McDermott, F., Tooth, A.F., 2001. High-resolution, multiple-trace-element variation in speleothems. J. Geol. Soc. Lond. 158, 831–841.

Fairchild, I.J., Smith, C.L., Baker, A., Fuller, L., Spötl, C., Mattey, D., McDermott, F., E.I.M.F., 2006. Modification and preservation of environmental signals in speleothems. Earth Sci. Rev. 75, 105–153.

Finch, A.A., Shaw, P.A., Weedon, G.P., Holmgren, K., 2001. Trace element variation in speleothem aragonite: potential for paleoenvironmental reconstruction. Earth Planet. Sci. Lett. 186, 255–267.

Flanagan, F.J., 1986. Reference samples in geology and geochemistry. U.S. Geological Survey Bulletin, 1582. Department of the Interior, US Government Printing Office.

Frisia, S., Borsato, A., Drysdale, R.N., Paul, B., Greig, A., Cotte, M., 2012. A re-evaluation of the palaeoclimatic significance of phosphorus variability in speleothems revealed by high-resolution synchrotron micro XRF mapping. Clim. Past 8, 2039–2051.

Frumkin, A., Stein, M., 2004. The Sahara–East Mediterranean dust and climate connection revealed by strontium and uranium isotopes in a Jerusalem speleothem. Earth Planet. Sci. Lett. 217, 451–464.

Gabitov, R.I., Watson, E.B., Sadekov, A., 2012. Oxygen isotope fractionation between calcite and fluid as a function of growth rate and temperature: an in situ study. Chem. Geol. 306–307, 92–102.

Hartland, A., Fairchild, I.J., Lead, J.R., Borsato, A., Baker, A., Frisia, S., Baalousha, M., 2012. From soil to cave: transport of trace metals by natural organic matter in karst dripwaters. Chem. Geol. 304–305, 68–82.

Hellstrom, J., Paton, C., Woodhead, J., Hergt, J., 2008. Iolite: Software for Spatially Resolved LA-(Quad and MC) ICPMS Analysis. Mineralogical Association of Canada Short Course, 40. Mineralogical Association of Canada, Vancouver, pp. 343–348.

Huang, H.M., Fairchild, I.J., Borsato, A., Frisia, S., Cassidy, N.J., McDermott, F., Hawkesworth, C.J., 2001. Seasonal variations in Sr, Mg and P in modern speleothems (Grotta di Ernesto, Italy). Chem. Geol. 175, 429–448.

Jochum, K.P., Scholz, D., Stoll, B., Weis, U., Wilson, S.A., Yang, Q., Schwalb, A., Börner, N., Jacob, D.E., Andreae, M.O., 2012. Accurate trace element analysis of speleothems and biogenic carbonates by LA-ICP-MS. Chem. Geol. 318–319, 31–44.

Johnson, R.A., Bhattacharyya, G.K., 2009. Statistics: Principles and Methods. John Wiley and Sons, Hoboken (704 pp.).

Johnson, K.R., Hu, C., Belshaw, N.S., Henderson, G.M., 2006. Seasonal trace-element and stable-isotope variations in a Chinese speleothem: the potential for high-resolution paleomonsoon reconstruction. Earth Planet. Sci. Lett. 2006, 394–407.

Kaufman, A., Wasserburg, G.J., Porcelli, D., Bar-Matthews, M., Ayalon, A., Halicz, L., 1998. U–Th isotope systematics from the Soreq cave, Israel and climatic correlations. Earth Planet. Sci. Lett. 156, 141–155.

Kaufman, A., Bar-Matthews, M., Ayalon, A., Carmi, I., 2003. The vadose flow above Soreq Cave, Israel: a tritium study of the cave waters. J. Hydro. 273, 155–163.

Kita, N.T., Ushikubo, T., Fu, B., Valley, J.W., 2009. High precision SIMS oxygen isotope analyses and the effect of sample topography. Chem. Geol. 264, 43–57.

Kolodny, Y., Bar-Matthews, M., Ayalon, A., McKeegan, K.D., 2003. A high spatial resolution $\delta^{18}O$ profile of a speleothem using an ion microprobe. Chem. Geol. 197, 21–28.

Kozdon, R., Ushikubo, T., Kita, N.T., Spicuzza, M., Valley, J.W., 2009. Intratest oxygen isotope variability in the planktonic foraminifer N. pachyderma: real vs. apparent vital effects by ion microprobe. Chem. Geol. 258, 327–337.

Kozdon, R., Kelly, D.C., Kita, N.T., Fournelle, J.H., Valley, J.W., 2011. Planktonic foraminiferal oxygen isotope analysis by ion microprobe technique suggests warm tropical sea surface temperatures during the Early Paleogene. Paleoceanography 26, PA3206.

Kuczumow, A.B., Vekemans, B., Schalm Wahnberg, P., Van Grieken, R., 2001. Analysis of speleothems by electron and X-ray microprobes. J. Anal. At. Spectrom. 16, 90–95.

Lachniet, M.S., 2009. Climatic and environmental controls on speleothem oxygen-isotope values. Quat. Sci. Rev. 28, 412–432.

MATLAB version 7.11.0.584. The MathWorks Inc., Natick, Massachusetts.

Mattey, D.P., Fairchild, I.J., Atkinson, T.C., Latin, J.-P., Ainsworth, M., Durell, R., 2010. Seasonal microclimate control of calcite fabrics, stable isotopes and trace elements in modern speleothem from St Michaels Cave, Gibraltar. Geol. Soc. Lond. Spec. Publ. 336, 323–344.

Matthews, A., Ayalon, A., Bar-Matthews, M., 2000. D/H ratios of fluid inclusions of Soreq Cave Israel speleothems as a guide to the Eastern Mediterranean Meteoric Line relationships in the last 120 ky. Chem. Geol. 166, 183–191.

McDermott, F., 2004. Palaeo-climate reconstructions from stable isotope variations in speleothems: a review. Quat. Sci. Rev. 23, 901–918.

McGarry, S.F., Bar-Matthews, M., Matthews, A., Vaks, A., Schilman, B., Ayalon, A., 2004. Constraints on hydrological and paleotemperature variations in the eastern Mediterranean region in the last 140 ka given by the δD values of speleothem fluid inclusions. Quat. Sci. Rev. 23, 919–934.

Mix, A.C., Ruddiman, W.F., McIntyre, A., 1986. Late Quaternary Paleoceanography of the tropical Atlantic, 2: the seasonal cycle of sea surface temperatures, 0–20,000 years B.P. Paleoceanography 1, 339–353.

O'Neil, J.R., Clayton, R.N., Mayeda, T.K., 1969. Oxygen fractionation in divalent metal carbonates. J. Chem. Phys. 51, 5547–5558.

Orland, I.J., Bar-Matthews, M., Kita, N.T., Ayalon, A., Matthews, A., Valley, J.W., 2009. Climate deterioration in the eastern Mediterranean as revealed by ion microprobe analysis of a speleothem that grew from 2.2 to 0.9 ka in Soreq Cave, Israel. Quat. Res. 71, 27–35.

Orland, I.J., Bar-Matthews, M., Ayalon, A., Matthews, A., Kozdon, R., Ushikubo, T., Valley, J.W., 2012. Seasonal resolution of Eastern Mediterranean climate change since 34 ka from a Soreq Cave speleothem. Geochim. Cosmochim. Acta 89, 240–255.

Paillard, D., Labeyrie, L, Yiou, P., 1996. Macintosh program performs time-series analysis. Eos Trans. AGU 77, 379.

Paton, C., Hellstrom, J., Paul, B., Woodhead, J., Hergt, J., 2011. Iolite: freeware for the visualization and processing of mass spectrometric data. J. Anal. At. Spectrom. 26, 2508–2518.

Rasband, W.S., 2012. ImageJ. U. S. National Institutes of Health, Bethesda, Maryland, USA (http://imagej.nih.gov/ij/).

Richards, D.A., Dorale, J.A., 2003. Uranium-series chronology and environmental applications of speleothems. Rev. Mineral. Geol. 52, 407–460.

Riechelmann, D.F.C., Deininger, M., Scholz, D., Riechelmann, S., Schröder-Ritzrau, A., Spötl, C., Richter, D.K., Mangini, A., Immenhauser, A., 2013. Disequilibrium carbon and oxygen isotope fractionation in recent cave calcite: comparison of cave precipitates and model data. Geochim. Cosmochim. Acta 103, 232–244.

Schimpf, D., Kilian, R., Kronz, A., Simon, K., Spötl, C., Wörner, G., Deininger, M., Mangini, A., 2011. The significance of chemical, isotopic, and detrital components in three coeval stalagmites from the superhumid southernmost Andes (53°S) as high-resolution palaeo-climate proxies. Quat. Sci. Rev. 30, 443–459.

Sokal, R.R., Rohlf, F.J., 1995. Biometry: the Principles and Practice of Statistics in Biological Research, 3rd edition. W.H. Freeman and Co, New York (887 pp.).

Treble, P., Shelley, J.M.G., Chappell, J., 2003. Comparison of high resolution sub-annual records of trace elements in a modern (1911–1992) speleothem with instrumental climate data from southwest Australia. Earth Planet. Sci. Lett. 216, 141–153.

Treble, P.C., Chappell, J., Shelley, J.M.G., 2005. Complex speleothem growth processes revealed by trace element mapping and scanning electron microscopy of annual layers. Geochim. Cosmochim. Acta 69, 4855–4863.

Tremaine, D.M., Froelich, P.N., Wang, Y., 2011. Speleothem calcite farmed in situ: modern calibration of $\delta^{18}O$ and $\delta^{13}C$ paleoclimate proxies in a continuously-monitored natural cave system. Geochim. Cosmochim. Acta 75, 4929–4950.

Tukey, J.W., 1977. Exploratory Data Analysis. Addison-Wesley Publishing Co., Reading.

Valley, J.W., Kita, N.T., 2009. In: Fayek, M. (Ed.), In situ Oxygen Isotope Geochemistry by Ion Microprobe. MAC short course: secondary ion mass spectrometry in the earth sciences, vol. 41, pp. 19–63.

von Storch, H., Zwiers, F.W., 1999. Statistical Analysis in Climate Research. Cambridge Univ. Press, Cambridge, UK (484 pp.).

Wassenburg, J.A., Immenhauser, A., Richter, D.K., Jochum, K.P., Fietzke, J., Deininger, M., Goos, M., Scholz, D., Sabaoui, A., 2012. Climate and cave control on Pleistocene/Holocene calcite-to-aragonite transitions in speleothems from Morocco: elemental and isotopic evidence. Geochim. Cosmochim. Acta 92, 23–47.

Weidel, B.C., Ushikubo, T., Carpenter, S.R., Kita, N.T., Cole, J.J., Kitchell, J.F., Pace, M.L., Valley, J.W., 2007. Diary of a bluegill (Lepomis macrochirus): daily $\delta^{13}C$ and $\delta^{18}O$ records in otoliths by ion microprobe. Can. J. Fish. Aquat. Sci. 64, 1641–1645.

Wong, C.I., Banner, J.L., Musgrove, M., 2011. Seasonal dripwater Mg/Ca and Sr/Ca variations driven by cave ventilation: Implications for and modeling of speleothem paleoclimate records. Geochim. Cosmochim. Acta 75, 3514–3529.